

24 **Silica polymorphs in lunar granite: Implications for granite petrogenesis on the Moon.**

25 Stephen M. Seddio, Randy L. Korotev, Bradley L. Jolliff, and Alian Wang.

26 Department of Earth and Planetary Sciences and McDonnell Center for the Space Sciences,

27 Washington University, St. Louis, Missouri 63130. (sseddio@levee.wustl.edu)

28

29

Abstract

30 Granitic lunar samples largely consist of granophyric intergrowths of silica and K-
31 feldspar. The identification of the silica polymorph present in the granophyre can clarify the
32 petrogenesis of the lunar granites. The presence of tridymite or cristobalite would indicate rapid
33 crystallization at high temperature. Quartz would indicate crystallization at low temperature or
34 perhaps intrusive, slow crystallization, allowing for the orderly transformation from high
35 temperature silica polymorphs (tridymite or cristobalite). We identify the silica polymorphs
36 present in four granitic lunar samples from the Apollo 12 regolith using laser-Raman
37 spectroscopy. Typically, lunar silica occurs with a hackle fracture pattern. We did an initial
38 density calculation on the hackle fracture pattern of quartz and determined that the volume of
39 quartz and fracture space is consistent with a molar volume contraction from tridymite or
40 cristobalite, both of which are less dense than quartz. Moreover, we analyzed the silica in the
41 granitic fragments from Apollo 12 by electron-probe microanalysis and found it contains up to
42 0.7 wt% TiO₂, consistent with initial formation as the high-temperature silica polymorphs, which
43 have more open crystal structures that can more readily accommodate cations other than Si. The
44 silica in Apollo 12 granitic samples crystallized rapidly as tridymite or cristobalite, consistent
45 with extrusive volcanism. The silica then inverted to quartz at a later time, causing it to contract
46 and fracture. A hackle fracture pattern is common in silica occurring in extrusive lunar

47 lithologies (e.g., mare basalt). The extrusive nature of these granitic samples makes them
48 excellent candidates to be similar to the rocks that compose positive relief silicic features such as
49 the Gruithuisen Domes.

50

51

Introduction

52 Among the Apollo samples and lunar meteorites, lunar granitic samples, also referred to
53 as “felsite,” are rare. In this paper, we use the adjective “granitic” to describe lithologies,
54 monomict or polymict, with a component of granophyric intergrowth of K-feldspar and silica
55 beyond blebs formed by silicate liquid immiscibility in the mesostasis of basalts. We reserve the
56 term “granite” for igneous lithologies that mostly consist of granophyre with accessory minerals
57 that have compositions consistent with extreme fractional crystallization (fayalite, hedenbergite).
58 Only 22 lunar samples have been identified to be granitic, accounting for less than 100 g total
59 mass (Seddio et al., 2013), <0.03% of the mass of all Apollo samples. Compared to terrestrial
60 rocks, silica minerals are rare in lunar samples and most commonly occur as accessory
61 concentrations of cristobalite or tridymite in mare basalts (Smith and Steele, 1976; Lucey et al.,
62 2006). Silica has been identified in basalts from all Apollo sites. Silica also has been identified in
63 gabbro (e.g., Sippel, 1971), microgabbro (Smith et al., 1970; Klein et al., 1971), monzogabbro
64 (e.g., Jolliff, 1991), ferroan anorthosite (Stewart et al., 1972), and granite (e.g., Seddio et al.,
65 2013; Seddio et al., 2014). The low-pressure silica polymorphs, quartz, tridymite, and
66 cristobalite, have been widely reported in lunar samples, but the high-pressure silica polymorphs
67 (coesite or stishovite) have been reported only rarely (Ohtani et al., 2011). The near absence of
68 coesite and stishovite is unexpected because these polymorphs are typically present in impact-
69 related rocks on Earth, and most of the lunar surface is saturated with craters. Papike et al. (1997)

70 suggested that absence of high-pressure silica polymorphs in lunar samples may result from the
71 paucity of silica minerals in the target rocks and the impact-induced volatilization of silica in
72 lunar surface environment.

73 Soon after the first Apollo samples were brought to Earth, Dence et al. (1970) and others
74 noted that the silica in the Apollo samples tended to exhibit a fracture pattern, which has been
75 described as “curved fractures” and as having a “cracked appearance” (Smith et al., 1970), or as
76 having a “crinkled texture” (Neal et al., 1994). In this work, we describe the fracture pattern of
77 silica as a “hackle” fracture pattern (Fig. 1). Fracturing within lunar silica has been used to
78 distinguish the polymorph as cristobalite (e.g., Ryder, 1976; Jolliff, 1991) and as “relict
79 cristobalite” (Jolliff et al., 1999). The latter identification assumes that the silica originally
80 crystallized as cristobalite and later underwent a molar volume contraction to quartz. Fracturing
81 in a silica phase has been used to identify which polymorph is present; however, because the
82 silica polymorph in a sample indicates the pressure and temperature conditions under which the
83 sample crystallized, it is important to determine the identity of a silica polymorph using an
84 analytical method, such as laser-Raman spectroscopy or laser-Raman imaging, that can directly,
85 and *in situ*, identify the structural form of a SiO₂ polymorph. The laser Raman spectra of quartz,
86 tridymite, and cristobalite are readily distinguishable from each other (Downs, 2006; Ling et al.,
87 2011).

88 The identification of the silica polymorph present in the granophyre can clarify the
89 petrogenesis of the lunar granites. Robinson and Taylor (2011) noted that if lunar granite
90 crystallized at depth (~10 km; Holmberg and Rutherford, 1994), where the conditions might
91 have been favorable for silicate-liquid immiscibility, and slow cooling may have allowed for
92 density separation of the complementary felsic and mafic liquids, the silica phase crystallizing

93 from the felsic liquid should have cooled slowly enough for quartz to form. Alternatively, if
94 silicic lava were to erupt at the lunar surface (i.e., at very low pressure), the silica should occur as
95 a high-temperature polymorph (tridymite, 870–1470°C, or cristobalite, 1470–1705°C; Holleman
96 and Wiberg, 1984; Rykart, 1995; Wenk and Bulakh, 2003).

97 A variety of techniques have been used to distinguish or identify the silica polymorphs
98 present within lunar samples, including optical petrography (e.g., Dence et al., 1970; Frondel et
99 al., 1970; Dollase et al., 1971; Sippel, 1971; Quick et al., 1981; Warren et al., 1983; Marvin et
100 al., 1991), electron diffraction (Champness et al., 1971), X-ray diffraction (e.g., Dence et al.,
101 1970; Frondel et al., 1970; Appleman et al., 1971; Dollase et al., 1971; Champness et al., 1971),
102 and laser-Raman spectroscopy (Jolliff et al., 1999; Robinson and Taylor, 2011; Seddio et al.,
103 2013; Seddio et al., 2014). Sippel and Spencer (1970) and Sippel (1971) identified and
104 distinguished between silica polymorphs; however, it is unclear whether the polymorphs were
105 identified using optical petrography or cathodoluminescence petrography. From a survey of the
106 literature, the silica polymorphs in 23 granitic samples have been identified or distinguished by
107 various means. Quick et al. (1981) identified quartz and tridymite in granitic breccia 12013 using
108 optical methods. Marvin et al. (1991) also used optical methods to distinguish quartz in “potash
109 rhyolite” 12070,102-5. Robinson and Taylor (2011) identified quartz as the silica polymorph in
110 19 granitic lunar samples using laser-Raman spectroscopy. Seddio et al. (2013) and Seddio et al.
111 (2014) identified quartz as the silica polymorph that occurs in granitic fragments 12032,366-19
112 and 12023,147-10, respectively, using laser-Raman spectroscopy. Here, we identify the silica
113 polymorphs present in 4 additional, recently characterized Apollo 12 granitic fragments using
114 laser-Raman spectroscopy imaging, and we interpret the laser-Raman spectroscopy data in

115 conjunction with the textures of the analyzed silica polymorphs and trace concentrations of non-
116 Si cations in the analyzed silica grains.

117

118 **Experimental methods**

119 Samples 12001,909-14, 12032,367-16, 12033,634-30, and 12033,634-34 are granitic
120 lithic fragments from the 2–4 mm grain-size fraction of the Apollo 12 regolith allocated for the
121 studies of Barra et al. (2006) and Korotev et al. (2011) along with 354 other lithic fragments. We
122 examined all 358 fragments under a binocular microscope and analyzed each one individually
123 for concentrations of 26 chemical elements by INAA (instrumental neutron activation analysis;
124 Korotev et al., 2011), including eight REEs (La, Ce, Nd, Sm, Eu, Tb, Yb, and Lu). Eight
125 fragments were found to be granitic in composition (high K, low Fe, high Th, and high U), with
126 12023,147-10 (Seddio et al., 2014) being the smallest at 2.67 mg.

127 We identified the silica polymorphs that occur in Apollo 12 granitic fragments
128 12001,909-14, 12032,367-16, 12033,634-30, and 12033,634-34 by laser-Raman spectroscopy
129 analysis using an inVia® Raman System (Renishaw) at Washington University. We obtained
130 laser-Raman spectroscopy data using both spot analysis mode and Streamline™ imaging mode.
131 The 532-nm line of a diode-pumped solid-state laser was used as the excitation source. Analyses
132 were done using a 50× long-working-distance objective (NA=0.5), which condenses the laser
133 beam into a spot of 1 μm diameter on the sample in spot analysis mode or into an elliptical spot
134 of 1 μm × 30 μm for the Streamline™ imaging mode. The objective also collects backscattered
135 Raman photons from the sample, which are sent to a Raman spectrometer through a width-
136 adjustable slit. A 2400 line/mm holographic grating disperses the collected Raman photons into a
137 Raman Stokes-shift range of 50 to 1300 cm⁻¹ for this study, with a spectral resolution of ~1 cm⁻¹.

138 Additional details of our laser-Raman spectroscopy analysis methodology can be found in Wang
139 et al. (2014).

140 We analyzed silica polymorphs for Na, Mg, Al, Si, P, K, Ti, Cr, and Fe by quantitative
141 wavelength-dispersive spectroscopy EPMA (electron-probe microanalysis) using the JEOL 8200
142 electron microprobe at Washington University. EPMA was done on sample 12023,147-10
143 (sample petrography and mineralogy described in Seddio et al., 2014) in addition to the four
144 samples that were analyzed by laser-Raman spectroscopy in this study. Analyses were done
145 using a 15 kV accelerating voltage and a 25 nA beam current. Na, Mg, Al, Si, P, K, Ca, Ti, Cr,
146 and Fe were counted on peak ($K\alpha$) for 52.5, 20, 35, 35, 30, 30, 30, 40, 20, and 30 seconds,
147 respectively (results and uncertainties in Table 1). Silica in sample 12032,367-16 has the highest
148 TiO_2 concentration among our silica-bearing lunar granitic samples. Many of the analysis spots
149 in 12032,367-16 are within 100 μm of an ilmenite grain, the Ti (and Fe) of which could be
150 fluoresced by Bremsstrahlung X-rays generated by the electron probe interacting with silica
151 (e.g., Wark and Watson, 2006). However, because the TiO_2 concentration is not correlated with
152 distance from the ilmenite grain, we are confident that the TiO_2 in the analyses is representative
153 of the SiO_2 phase in sample 12032,367-16.

154 In order to investigate whether the hackle fracture pattern (e.g., Fig. 1) present in some
155 silica occurrences formed by a molar volume contraction caused by a lower density polymorph
156 (tridymite or cristobalite) changing to a higher density polymorph (quartz), we used SE
157 (secondary electron) images to calculate fracture area and silica area (A_{Frac} and A_{Qtz} ,
158 respectively). We assume that the fracture and silica areas in the images are representative of the
159 fracture and silica volumes (V_{Frac} and V_{Qtz} , respectively). The density of the higher temperature

160 polymorph—the silica polymorph that originally crystallized—can be calculated using the
161 following method:

$$\rho_{HighT} = \rho_{Qtz} \frac{V_{Qtz}}{V_{HighT}} \cong \rho_{Qtz} \frac{A_{Qtz}}{A_{HighT}} = \rho_{Qtz} \frac{A_{Qtz}}{A_{Qtz} + A_{Frac}}$$

162 which we refer to hereafter as the initial density calculation. We used BSE (backscattered
163 electron) images to confirm the location of boundaries between silica and other phases. Images
164 were made using an accelerating voltage of 15 kV and a probe current of 1 nA to minimize spot
165 size. In addition to the aforementioned granitic lunar samples, we used the initial density
166 calculation to calculate the initial density of the quartz exhibiting a hackle fracture pattern in
167 Apollo 12 granite fragment 12032,366-19 (characterized in Seddio et al., 2013).

168 We determined modal abundances for four granitic fragments. Phase abundances were
169 determined using image analysis of BSE mosaics and X-ray maps to essentially count all pixels
170 of each phase, which we then divided by the total number of pixels (background subtracted) to
171 obtain the area fraction, which we take to be proportional to the volume fraction. Based on
172 counting statistics, the error associated with the modal abundances of major and accessory
173 phases is typically <1%; the error associated with the modal abundances of trace phases is
174 typically <30%. The error associated with trace phases is high because, in the BSE images and
175 X-ray maps, these phases are represented by as few as 12 pixels each (the total sample areas are
176 represented by millions of pixels).

177

178 **Sample 12001,909-14**

179 Sample 12001,909-14 is a 7.01 mg complex polymict granitic breccia (Fig. 2). We
180 describe the petrography of sample 12001,909-14 in terms of seven areas (Fig. 3) on the basis of
181 textures and mineral compositions. The modal abundances of the phases within the seven areas

182 are in Table 2. The ranges of end-member compositions and average compositions for the major
183 minerals in Areas 1 and 2, Areas 3 and 4, Areas 5 and 6 and Area 7 are in Tables 3, 4, 5, and 6,
184 respectively. Individual analyses for the major minerals in all areas of sample 12001,909-14 are
185 in Appendix 1. Area 1 is a 1×0.75 mm rounded clast of basaltic impact melt and accounts for
186 23% of the section. Area 2 accounts for 2.4% of sample 12001,909-14 and comprises four
187 rounded basaltic impact melt clasts, the largest of which is 0.2×0.4 mm. The most distinct
188 difference between Areas 1 and 2 is that Area 2 contains more K-feldspar. Area 3 accounts for
189 6.6% of the section and comprises mineral fragments in a granophyre matrix. Area 4, 15% of the
190 sample, is similar to Area 3 but contains less pyroxene. Area 5 accounts for 26% of the sample,
191 and Area 6 represents 19%. Most of the high-Ca pyroxene in Area 6 occurs as a 0.15×0.2 mm
192 zoned grain (core: $\text{En}_{-10}\text{Wo}_{-41}\text{Fs}_{-49}$, rim: $\text{En}_{-34}\text{Wo}_{-39}\text{Fs}_{-27}$; Figs. 2 and 4). Area 7 accounts for
193 8% of sample 12001,909-14. A trace amount of high-Ca pyroxene is present in Area 7, as fine
194 ($\sim 1 \mu\text{m}$) exsolution lamellae in the low-Ca pyroxene. We are unable to analyze the exsolution
195 lamellae of high-Ca pyroxene without sampling the adjacent low-Ca pyroxene, but we presume
196 that the composition of the Area 7 high-Ca pyroxene is similar ($\text{En}_{32-37}\text{Wo}_{\sim 39}\text{Fs}_{26-43}$) to that in the
197 rest of sample 12001,909-14 (except the large zoned high-Ca pyroxene in Area 6) because the
198 high- and low-Ca pyroxene compositions are homogenous throughout the sample.

199 The granophyre in Area 7 is different from that found in the rest of the sample. The Area 7
200 silica is not fractured whereas the silica in the other areas exhibits a hackle fracture pattern (e.g.,
201 Fig. 5). The intergrowths of K-feldspar and silica in Area 7 are approximately twice as wide as
202 the intergrowths in the other areas. Additionally, the K-feldspar in Area 7 has the highest Cn
203 content (“Cn” refers to celsian—the Ba-feldspar end-member) in the sample (as high as $\text{Cn}_{5.1}$);

204 whereas Area 6 K-feldspar has $Cn_{<4}$, and the rest of the K-feldspar in sample 12001,909-14 has
205 $Cn_{<3}$.

206 **Sample 12032,367-16**

207 Sample 12032,367-16 is a 7.80 mg friable, strongly fractured granitic breccia consisting
208 of 41.8% plagioclase, 24.3% silica, 18.7% low-Ca pyroxene, 14.1% K-feldspar, 0.6% apatite,
209 0.3% ilmenite, and 0.2% zircon with trace amounts of zirconolite. The ranges of end-member
210 compositions and average compositions for the major minerals in sample 12032,367-16 are in
211 Table 7. Individual analyses of the major minerals in sample 12032,367-16 are in Appendix 2. In
212 the portions of the sample where the granophyre occurs, it consists of K-feldspar intergrown with
213 fracture-free silica occurring in the interstices between blocky plagioclase grains (Fig. 6 inset).

214

215 **Sample 12033,634-30**

216 Sample 12033,634-30 is a 7.50 mg monomict granitic breccia (Fig. 7) consisting of
217 31.3% plagioclase, 20.6% silica with a hackle fracture pattern, 18.4% high-Ca pyroxene, 16.5%
218 K-feldspar, 8.3% low-Ca pyroxene, 2.0% RE-merrillite, 1.5% apatite, 1.1% ilmenite, 0.2%
219 zircon, and trace amounts of olivine (one grain) and troilite (two grains). The ranges of end-
220 member compositions and average compositions for the major minerals in sample 12033,634-30
221 are in Table 8. Individual analyses of the major minerals in sample 12033,634-30 are in
222 Appendix 3. The sample is composed of angular and sub-rounded mineral fragments in a
223 granophyric matrix of K-feldspar and silica. One corner of the section (right corner of the
224 fragment in Fig. 7) contains a significantly higher proportion of granophyre compared to the rest
225 of the sample. This area also contains the only occurrence of fayalitic olivine. The largest
226 pyroxene grain is intergrown with apatite.

227

228 **Sample 12033,634-34**

229 Sample 12033,634-34 is a 6.96 mg granite (Fig. 8) comprising 30.3% ternary feldspar,
230 24.0% silica, 21.1% K-feldspar, 8.7% pyroxene, 7.1% fayalitic olivine, 4.0% apatite, 3.9% RE-
231 merrillite, 1.0% ilmenite, and trace amounts of plagioclase, zirconolite, zircon, and baddeleyite.
232 The ranges of end-member compositions and average compositions for the major minerals in
233 sample 12033,634-34 are in Table 9. Individual analyses of the major minerals in sample
234 12033,634-34 are in Appendix 4. Some grains of fayalite, K-feldspar, ternary feldspar, and,
235 quartz are large enough to be visible with the unaided eye and are all irregularly shaped. The
236 large fayalite grain in Figure 8 is strongly fractured. Three silica grains are > 0.1 mm and have
237 curved boundaries. Pyroxene is typically zoned and elongate with parallel fractures oriented
238 perpendicular to the direction of grain elongation. The remainder of sample 12033,634-34
239 consists primarily of granophyric intergrowths of silica and K-feldspar, the grains of which are in
240 some cases < 1 mm in maximum dimension.

241

242

Results

243 Using laser-Raman spectroscopy, we identified quartz in samples 12001,909-14,
244 12033,634-30, and 12033,634-34; cristobalite in sample 12032,367-16; and amorphous silica in
245 sample 12001,909-14. Examples of Raman spectra from quartz-bearing samples are shown in
246 Figure 9, and peak positions used to identify phases are listed in Table 10. Figures 10 and 11
247 show examples of Raman spectra from a cristobalite-bearing sample and the amorphous SiO₂-
248 bearing sample, respectively. In sample 12001,909-14, Areas 3, 4, 5, and 6 contain quartz, all of
249 which have a hackle fracture pattern; however, Area 7 contains amorphous silica that does not

250 have a hackle fracture pattern. Sample 12032,367-16 contains cristobalite without a hackle
251 fracture pattern. Samples 12023,147-10, 12033,634-30, and 12033,634-33 contain quartz with a
252 hackle fracture pattern.

253 Because, compared to quartz, the relatively more open crystal structures of tridymite and
254 cristobalite can better accommodate cations other than Si (Papike and Cameron, 1976; Smith and
255 Steele, 1984), the measurement of trace or minor concentrations of other cations can aid with the
256 identification of the silica polymorph present. The results of the EPMA for minor elements (Ti,
257 Al, Cr, Fe, Mg, Ca, Na, K, and P) in silica of lunar granite are summarized in Table 1 and Figure
258 12. Because the silica grains in the lunar granitic samples of this study are typically only a few
259 micrometers wide, most of the Na₂O, Al₂O₃, K₂O, and CaO present in the analyses are
260 attributable to overlap of the electron probe interaction volume with adjacent feldspar (yielding
261 Na, Al, K, and Ca) or the secondary fluorescence from characteristic Si X-rays (yielding Na and
262 Al).

263 The results of the initial density calculation of the quartz with a hackle fracture pattern
264 are summarized in Table 11. The initial silica densities that we calculate from quartz (density:
265 2.65 g/cm³; Will et al., 1988) with a hackle fracture pattern in the six (including samples
266 12023,147-10 and 12032,366-19) granitic lunar samples that we have studied are similar to the
267 densities of the high-temperature, low-pressure silica polymorphs (tridymite, density: 2.18–2.28
268 g/cm³; Kihara, 1978; and cristobalite, density: 2.32–2.36 g/cm³; Schmahl et al., 1992). The initial
269 silica densities are most consistent with tridymite, except in sample 12033,634-34, which has an
270 initial density calculation most like that of cristobalite.

271

272

Discussion

273 In lunar granitic lithologies, the silica polymorphs quartz, cristobalite, and tridymite, as
274 well as amorphous silica, have been identified (Quick et al., 1981; Robinson and Taylor, 2011;
275 Seddio et al., 2013). Typically, quartz is the silica polymorph intergrown with K-feldspar or
276 plagioclase in lunar granite. In granitic lunar samples, all silica that has been identified as quartz
277 using laser-Raman spectroscopy has a hackle fracture pattern. Moreover, all silica with a hackle
278 fracture pattern in the samples that we have studied has been found definitively to be quartz. In
279 granitic lunar samples, cristobalite and amorphous silica have not been observed to occur with
280 the distinctive hackle fracture pattern. Tridymite has only been reported in granitic breccia 12013
281 (optically identified by Quick et al., 1981). Appendix 5 contains a survey of all lunar samples
282 that contain silica and what polymorphs have been identified therein.

283 The fractured nature of lunar silica has been interpreted to result from a molar volume
284 inversion. Dence et al. (1970) and Smith et al. (1970) attributed fractures in cristobalite—
285 identified optically and by X-ray diffraction—to an inversion from high to low cristobalite.
286 However, because quartz is the silica polymorph typically found in granitic lunar samples, we
287 attribute the hackle fracture pattern of quartz in granitic lunar samples to a molar volume
288 inversion from cristobalite (density: 2.32–2.36 g/cm³; Schmahl et al., 1992) or tridymite (density:
289 2.18–2.28 g/cm³; Kihara, 1978) to quartz (density: 2.65 g/cm³; Will et al., 1988) on the basis of
290 the initial density calculation. Inverting from a lower to a higher density phase would produce
291 isotropic tensional stress within the quartz, causing it to fracture (i.e., the hackle pattern). This
292 process of fracturing is similar, but greater in magnitude, to that fracturing that can occur with
293 the transition of β - to α -cristobalite (e.g., Carpenter et al., 1998; Damby et al., 2014).

294 Inversion of tridymite or cristobalite to quartz is a reconstructive phase transition (e.g.,
295 Lakshatanov et al., 2007), requiring reconfiguration of Si–O bonds. Although this inversion
296 might be constrained (as opposed to a displacive transformation), we think that transformation of
297 a high-temperature silica polymorph to quartz is the best explanation for the hackle fracture
298 patterns observed in the quartz of granitic lunar samples. Perhaps this transformation was aided
299 by impact-induced heating events experienced by granitic samples resulting in their excavation
300 and possibly other impact events during their >3 Ga history.

301 The Raman spectra collected from lunar quartz all have peaks that are shifted to lower
302 positions from the typical quartz peak positions (Table 10; Fig. 9). This red shift is a result of
303 stress within the SiO₂ structural framework and has been attributed to shock metamorphism
304 (McMillan et al., 1992; Ling et al., 2011). A result of the experiments of McMillan et al. (1992)
305 is that the major peak position of unshocked quartz (464 cm⁻¹) is shifted down to 455 cm⁻¹ after
306 shock to a peak pressure of 31.4 GPa. Additionally, the magnitude of the peak shift in the quartz
307 Raman spectrum is directly, but not linearly, related to the magnitude of shock pressure
308 experienced by a sample (McMillan et al., 1992). Based on this relationship, the granites in this
309 study, which exhibit a maximum peak shift down to 460 cm⁻¹ (sample 12033,634-34; Table 10)
310 from unshocked quartz (464 cm⁻¹), should not have experienced shock pressures greater than ~25
311 GPa. An alternative explanation of the peak shift of the Raman spectra of quartz in this study is
312 that the fracturing of the quartz after inversion from a phase of higher density did not perfectly
313 relieve the stress within the silica. Perhaps this remnant stress may be responsible for the
314 observed shift of the peaks in the Raman spectra of quartz with a hackle fracture pattern.

315 Compared to quartz, tridymite and cristobalite can incorporate greater amounts of cations
316 other than Si—typically, Na, Al, K, Ti, and Fe (Fig. 12)—into their relatively open crystal

317 structures (Papike and Cameron, 1976; Smith and Steele, 1984). In tridymite and cristobalite, Si
318 substitution typically involves Al^{3+} replacing Si^{4+} with charge balance maintained by the
319 introduction of Na^+ or K^+ into interstitial vacancies (Papike and Cameron, 1976). Smith and
320 Steele (1984) reported Na, Al, K, and Ti abundances in samples of terrestrial quartz, tridymite,
321 and cristobalite samples (5, 4, and 1 samples, respectively). Because our Na, Al, and K data
322 likely include a contribution from neighboring feldspars, we are only confident comparing our Ti
323 data to the data of Smith and Steele (1984), who reported 0.06–0.22 wt% TiO_2 in tridymite, and
324 <0.01 wt% TiO_2 in quartz. In the lunar granitic samples containing quartz and amorphous silica,
325 TiO_2 concentrations are within the range of concentrations that Smith and Steele (1984) report
326 for tridymite. However, the cristobalite we identified in sample 12032,367-16 contains 0.30–0.67
327 wt% TiO_2 (Fig. 12).

328 The occurrence of quartz as the silica polymorph in lunar granite has been interpreted to
329 mean that quartz-bearing lunar granite crystallized at depth (Robinson and Taylor, 2011). If
330 crystallization occurred at a depth where the pressure was sufficiently high, the parent magma
331 could have crystallized quartz. Alternatively, if crystallization occurred at depth but at pressures
332 low enough and temperatures high enough for the primary crystallization of tridymite or
333 cristobalite, perhaps slow cooling may have permitted orderly transformations from high-
334 temperature polymorphs to quartz. The neighboring phases may have been warm enough to
335 accommodate the volume changes associated with the structural inversions occurring in silica.
336 However, because the majority of lunar granite samples contain quartz with a hackle fracture
337 pattern, it is more likely that quartz-bearing lunar granite crystallized rapidly at high temperature,
338 with primary crystallization and preservation of tridymite or cristobalite as the silica polymorph
339 until a structural inversion occurred at some later time, causing a reduction in molar volume. The

340 petrographic evidence for the crystallization of silica as a high-temperature polymorph—
341 tridymite or cristobalite—is supported by high TiO₂ concentrations. Furthermore, the small (<1
342 mm) grain sizes that typically occur in lunar granites indicate rapid crystallization, in comparison
343 to other lunar primary igneous rocks that exhibit coarser grain sizes. Sample 15405,12 is an
344 exception, with grain sizes > 1 mm, silica with a hackle fracture pattern, and is interpreted to
345 have crystallized in a pluton (Ryder, 1976). In sample 12033,634-34, some grain sizes are > 1
346 mm, but irregular grain sizes and ternary feldspar are indicative of rapid crystallization.

347

348

Implications

349 The silica polymorph contained in lunar granite is most commonly quartz. These quartz
350 grains typically exhibit a hackle fracture pattern indicating that they inverted from a high-
351 temperature, low-pressure polymorph, either tridymite or cristobalite. The preservation of high-
352 temperature silica polymorphs, before a molar volume contraction to quartz at some point later,
353 and the fine-grained textures of most granitic lunar samples indicate that that the samples
354 experienced relatively rapid cooling (e.g., rhyolitic volcanism). Laser-Raman spectroscopy is
355 very sensitive to the differences in structure and symmetry of the silica polymorphs and is thus a
356 well-suited method to identify, unambiguously and *in situ*, the silica polymorph(s) present in
357 granitic lunar samples. The laser-Raman spectroscopy spectra, coupled with textural and
358 compositional data, provide a clear indication of the crystallization of the silica polymorphs and
359 a firm constraint on crystallization conditions.

360 The Apollo 12 granitic samples of this study contain silica that we identified using laser-
361 Raman spectroscopy to be cristobalite, amorphous silica, or quartz with a hackle fracture pattern.

362 The EPMA measurements of the silica in the Apollo 12 granitic samples are consistent with

363 analyses of high-temperature silica polymorphs. The initial density calculations of quartz with a
364 hackle fracture pattern in Apollo 12 granites indicate that the silica crystallized as a high-
365 temperature polymorph. We conclude that the Apollo 12 granitic samples must have crystallized
366 at a temperature above 870° C and that they did so rapidly enough to preserve the high-
367 temperature polymorph. The fine-grained nature of the granitic samples also indicates rapid
368 crystallization. Rapid crystallization from high temperature suggests that the Apollo 12 granitic
369 samples are a product of extrusive magmatism.

370 Granitic lunar samples are silicic and have the highest Th concentrations among known
371 lunar lithologies (e.g., Seddio et al., 2013). Some locations on the Moon are also known to be
372 silicic based on orbital radiometry (Glotch et al., 2010) and rich in Th based on orbital gamma-
373 ray spectroscopy (e.g., Lawrence et al., 2003; Hagerty et al., 2006; Jolliff et al., 2011), such as
374 the Gruithuisen Domes and the Mairan Domes. This compositional similarity has led to the
375 interpretation that granitic lunar samples might represent volcanic exposures similar to these
376 domes.

377

378

Acknowledgements

379 This work was funded by NASA grant NNX11AJ66G (RLK) and NASA MFRP grant
380 NNX10AM89G (AW). We thank Allan Treiman, Marc Freis, and Associate Editor Steven
381 Simon for their insightful reviews that improved this paper. Additionally, we thank Axel
382 Wittmann for helpful comments.

383

384

References cited

385 Appleman, D.E., Nissen, H.-U., Stewart, D.B., Clark, J.R., Dowty, E., and Huebner, J.S. (1971)

386 Studies of lunar plagioclase, tridymite, and cristobalite. Proceedings of the 2nd Lunar
387 Science Conference, 1, 117–133.

388 Barra, F., Swindle, T.D., Korotev, R.L., Jolliff, B.L., Zeigler, R.A., and Olson, E. (2006)

389 ⁴⁰Ar-³⁹Ar dating on Apollo 12 regolith: Implications on the age of Copernicus and the
390 source of non-mare materials. *Geochimica et Cosmochimica Acta*, 70, 6016–6031.

391 Carpenter, M.A., Salje, E.K.H., and Graeme-Barber, A. (1998) Spontaneous strain as a

392 determinant of thermodynamic properties for phase transitions in minerals. *European*
393 *Journal of Mineralogy*, 10, 621–691.

394 Champness, P.E., Dunham, A.C., Gibb, F.G.F., Giles, H.N., MacKenzie, W.S., Stumpfl, E.F.,

395 and Zussman, J. (1971) Mineralogy and petrology of some Apollo 12 lunar samples.
396 Proceedings of the 2nd Lunar Science Conference, 1, 359–376.

397 Damby, D.E., Llewelin, E.W., Horwell, C.J., Williamson, B.J., Najorka, J., Cressey, G., and

398 Carpenter, M. (2014) The α - β phase transition in volcanic cristobalite. *Journal of Applied*
399 *Crystallography*, 47, 1205–1215.

400 Dence, M.R., Douglas, J.A.V., Plant, A.G., and Traill, R.J. (1970) Petrology, mineralogy and

401 deformation of Apollo 11 samples. Proceedings of the Apollo 11 Lunar Science
402 Conference, 1, 315–340.

403 Dollase, W.A., Cliff, R.A., and Wetherill, G.W. (1971) Note on tridymite in rock 12021.

404 Proceedings of the 2nd Lunar Science Conference, 1, 141–142.

- 405 Downs, R.T. (2006) The RRUFF Project: an integrated study of the chemistry, crystallography,
406 Raman and infrared spectroscopy of minerals. Program and Abstracts of the 19th general
407 meeting of the International Mineralogical Association in Kobe, Japan, O03–13.
- 408 Frondel, C., Klein Jr., C., Ito, J., and Drake, J.C. (1970) Mineralogical and chemical studies of
409 Apollo 11 lunar fines and selected rocks. Proceedings of the Apollo 11 Lunar Science
410 Conference, 1, 445–474.
- 411 Glotch, T.D., Lucey, P.G., Bandfield, J.L., Greenhagen, B.T., Thomas, I.R., Elphic, R.C.,
412 Bowles, N., Wyatt, M.B., Allen, C.C., Hanna, K.D., Paige, D.A. (2010) Highly silicic
413 compositions on the Moon. *Science*, 329, 1510.
- 414 Hagerty, J.J., Lawrence, D.J., Hawke, B.R., Vaniman, D.T., Elphic, R.C., and Feldman, W.C.
415 (2006) Refined thorium abundances for lunar red spots: Implications for evolved,
416 nonmare volcanism on the Moon. *Journal of Geophysical Research*, 111, E06002.
- 417 Holleman, A.F. and Wiberg, E. (1984) *Lehrbuch Der Anorganischen Chemie*. Berlin, New York:
418 Walter Gruyter Verlag, ISBN 3-11-007511-3.
- 419 Holmberg, B. and Rutherford, M.J. (1994) An experimental study of KREEP basalt evolution.
420 Abstracts of the 25th Lunar and Planetary Science Conference, 557.
- 421 Jolliff, B.L. (1991) Fragments of quartz monzodiorite and felsite in Apollo 14 soil particles.
422 Proceedings of Lunar and Planetary Science Conferences, 21, 101–118.
- 423 Jolliff, B.L., Floss, C., McCallum, I.S., and Schwartz, J.M. (1999) Geochemistry, petrology, and
424 cooling history of 14161,7373: A plutonic lunar sample with textural evidence of
425 granitic-fraction separation by silicate-liquid immiscibility. *American Mineralogist*, 84,
426 821–837.

- 427 Jolliff, B.L., Wiseman, S.A., Lawrence, S.J., Tran, T.N., Robinson, M.S., Sato, H., Hawke, B.R.,
428 Scholten, F., Oberst, J., Hiesinger, H., van der Bogert, C.H., Greenhagen, B.T., Glotch,
429 T.D., and Paige, D.A. (2011) Non-mare silicic volcanism on the lunar farside at
430 Compton-Belkovich. *Nature Geoscience*, 4, 566–571.
- 431 Kihara, K. (1978). Thermal change in unit-cell dimensions, and a hexagonal structure of
432 tridymite. *Zeitschrift für Kristallographie*, 148, 237–253.
- 433 Klein, Jr., C., Drake, J.C., and Frondel, C. (1971) Mineralogical, petrological, and chemical
434 features of four Apollo 12 lunar microgabbros. *Proceedings of the 2nd Lunar Science*
435 *Conference*, 1, 265–284.
- 436 Korotev, R.L., Jolliff, B.L., Zeigler, R.A., Seddio, S.M., and Haskin, L.A. (2011) Apollo 12
437 revisited. *Geochimica et Cosmochimica Acta*, 75, 1540–1573.
- 438 Lawrence, D.J., Elphic, R.C., Feldman, W.C., Prettyman, T.H., Gasnault, O., and Maurice, S.
439 (2003) Small-area thorium features on the lunar surface. *Journal of Geophysical*
440 *Research*, 108, 5102.
- 441 Lakshtanov, D.L., Sinogeikin, S.V., and Bass, J.D. (2007) High-temperature phase transitions
442 and elasticity of silica polymorphs. *Physics and Chemistry of Minerals*, 34, 11–22.
- 443 Ling, Z.C., Wang, A., and Jolliff, B.L. (2011) Mineralogy and geochemistry of four lunar soils
444 by laser-Raman study. *Icarus*, 211, 101–113. doi:10.1016/j.icarus.2010.08.02.
- 445 Lucey, P., Korotev, R.L., Gillis, J.J., Taylor, L.A., Lawrence, D., Campbell, B.A., Elphic, R.,
446 Feldman, B., Hood, L.L., Hunten, D., Mendillo, M., Noble, S., Papike, J.J., Reedy, R.C.,
447 Lawson, S., Prettyman, T., Gasnault, O., and Maurice, S. (2006) Understanding the lunar
448 surface and space-Moon interactions. *Reviews in Mineralogy and Geochemistry*, 60, 83–
449 219.

- 450 Marvin, U.B., Lindstrom, M.M., Holmberg, B.B., and Martinez, R.R. (1991) New observations
451 on the quartz monzodiorite-granite suite. Proceedings of Lunar and Planetary Science
452 Conference, 21, 119–135.
- 453 McMillan, P.F., Wolf, G.H., and Lambert, P. (1992) A Raman-spectroscopic study of shocked
454 single crystalline quartz. Physics and Chemistry of Minerals, 19, 71–79.
- 455 Neal, C.R., Hacker, M.D., Snyder, G.A., Taylor, L.A., Liu, Y.-G., and Schmitt, R.A. (1994)
456 Basalt generation at the Apollo 12 site, part 1: New data, classification, and re-evaluation.
457 Meteoritics, 28, 334–338.
- 458 Ohtani, E., Ozawa, S., Miyahara, M., Ito, Y., Mikouchi, T., Kimura, M., Sato, K., and Hiraga, K.
459 (2011) Coesite and stishovite in a shocked lunar meteorite, Asuka-881757, and impact
460 events in lunar surface. Proceedings of the National Academy of Sciences, 108(2), 463–
461 466.
- 462 Papike, J.J. and Cameron, M. (1976) Crystal chemistry of silicate minerals of geophysical
463 interest. Reviews of Geophysics and Space Physics, 14, 37–80.
- 464 Papike, J.J., Spilde, M.N., Adcock, C.T., Fowler, G.W., and Shearer, C.K. (1997) Trace element
465 fractionation by impact-induced volatilization: SIMS study of lunar HASP Samples.
466 American Mineralogist, 82, 630–634.
- 467 Quick, J.E., James, O.B., and Albee, A.L. (1981) Petrology and petrogenesis of lunar breccia
468 12013. Proceedings of Lunar and Planetary Science Conference, 12, 117–172.
- 469 Robinson, K.L. and Taylor, G.J. (2011) Intrusive and extrusive lunar felsites. Lunar and
470 Planetary Science Conference *XLII*, Abstract #1257.
- 471 Ryder, G. (1976) Lunar sample 15405: remnant of a KREEP basalt-granite differentiated pluton.
472 Earth and Planetary Science Letters, 29, 255–268.

- 473 Rykart, R. (1995) Quarz-Monographie: Die Eigenheiten von Bergkristall, Rauchquarz,
474 Amethyst, Chalcedon, Achat, Opal und anderen Varietäten. Thun-Ott Verlag, 2nd. Ed.,
475 ISBN 3-7225-6204-X
- 476 Schmahl, W.W., Swainson, I.P., Dove, M.T., and Graeme-Barber, A. (1992). Landau free energy
477 and order parameter behaviour of the α/β phase transition in cristobalite. Zeitschrift für
478 Kristallographie, 201, 125–145.
- 479 Seddio, S.M., Jolliff, B.L., Korotev, R.L., and Zeigler, R.A. (2013) Petrology and geochemistry
480 of lunar granite 12032,366-19 and implications for lunar granite petrogenesis. American
481 Mineralogist, 98, 1697–1713.
- 482 Seddio, S.M., Jolliff, B.L., Korotev, R.L., and Carpenter, P.K. (2014) Thorite in an Apollo 12
483 granite fragment and age determination using the electron microprobe. Geochimica et
484 Cosmochimica Acta, 135, 307–320.
- 485 Sippel, R.F. and Spencer, A.B. (1970) Luminescence petrography and properties of lunar
486 crystalline rocks and breccias. Proceedings of the Apollo 11 Lunar Science Conference,
487 1, 2413–2426.
- 488 Sippel, R.F. (1971) Luminescence petrography of the Apollo 12 rocks and comparative features
489 in terrestrial rocks and meteorites. Proceedings of the 2nd Lunar Science Conference, 1,
490 247–263.
- 491 Smith, J.V., Anderson, A.T., Newton, R.C., Olsen, E.J., and Wyllie, P.J. (1970) Petrologic
492 history of the moon inferred from petrography, mineralogy and petrogenesis of Apollo 11
493 rocks. Proceedings of the Apollo 11 Lunar Science Conference, 1, 897–925.
- 494 Smith, J.V. and Steele, I.M. (1976) Lunar mineralogy: a heavenly detective story. Part II.
495 American Mineralogist, 61, 1059–1116.

- 496 Smith, J.V. and Steele, I.M. (1984) Chemical substitution in silica polymorphs. Neues Jahrbuch
497 fuer Mineralogie, Monatshefte, H. 3, 137–144.
- 498 Stewart, D.B., Ross, M., Morgan, B.A., Appleman, D.E., Huebner, J.S., Commeau, R.F. (1972)
499 Mineralogy and Petrology of Lunar Anorthosite 15415. Abstracts of the 3rd Lunar
500 Science Conference, 726.
- 501 Wang, A., Korotev, R.L., Jolliff, B.L., and Ling, Z.C. (2014) Raman imaging of extraterrestrial
502 materials. Planetary and Space Science, accepted. doi:10.1016/j.pss.2014.10.005.
- 503 Wark, D.A. and Watson, E.B. (2006) TitaniQ: a titanium-in-quartz geothermometer.
504 Contributions to Mineralogy and Petrology, 152, 743–754.
- 505 Warren, P.H., Taylor, G.J., Keil, K., Shirley, D.N., and Wasson, J.T. (1983) Petrology and
506 chemistry of two 'large' granite clasts from the moon. Earth and Planetary Science
507 Letters, 64, 175–185.
- 508 Wenk, H.-R. and Bulakh, A. (2003) Minerals: Their Constitution and Origin, Cambridge:
509 Cambridge University Press, ISBN 0-521-52958-1.
- 510 Will, G., Bellotto, M., Parrish, W., and Hart, M. (1988). Crystal structures of quartz and
511 magnesium germanate by profile analysis of synchrotron-radiation high-resolution
512 powder data. Journal of Applied Crystallography, 21, 182–191.

513 **Figure 1.** a) BSE (backscattered electron) image and b) SE (secondary electron) image of quartz
514 with a hackle fracture pattern in 12023,147-10.

515
516

517 **Figure 2.** BSE (backscattered electron) image of 12001,909-14. In order of brightness from
518 darkest to brightest, minerals (or phases) are quartz, amorphous silica, plagioclase, K-feldspar,
519 high-Ca pyroxene, low-Ca pyroxene, ilmenite, and zircon. Zirconolite and monazite also occur
520 but the grains are too small to resolve in this image. The white rectangle highlights the zoned
521 0.15×0.2 mm high-Ca pyroxene grain (core: $\text{En}_{\sim 10}\text{Wo}_{\sim 41}\text{Fs}_{\sim 49}$, rim: $\text{En}_{\sim 34}\text{Wo}_{\sim 39}\text{Fs}_{\sim 27}$). See Fig. 4
522 for a high resolution BSE image, X-ray maps, and a laser-Raman image of the zoned pyroxene
523 grain.

524
525

526 **Figure 3.** Locations of seven areas in sample 12001,909-14 that were identified based on
527 petrographic similarities.

528
529

530 **Figure 4.** Images of the zoned high-Ca pyroxene grain in Area 6 of 12001,909-14. The core has
531 a composition of $\text{En}_{10}\text{Wo}_{41}\text{Fs}_{49}$; the rim has a composition of $\text{En}_{34}\text{Wo}_{39}\text{Fs}_{27}$. **a.** Backscattered
532 electron image in which zoning is evidenced by brighter core and darker rim. **b.** Ca, Mg, and Fe
533 X-ray maps merged into an RGB image. The purple core indicates hedenbergite, and the yellow-
534 green rim is the more magnesian high-Ca pyroxene. Teal is low-Ca pyroxene—a reaction
535 product of fayalite with surrounding quartz and the magnesian lithology. Fayalite occurs with
536 quartz and K-feldspar in an inclusion that crystallized from late-stage melt. Inclusions of
537 fayalite+K-feldspar+quartz also occur in hedenbergite in lunar granite 12032,366-19 (Seddio et
538 al., 2013). Blue specks are ilmenite. Teardrop-shaped inclusion is K+Si glass surrounding Ca-
539 phosphosphate (red speck). **c.** Laser-Raman image in which white, yellow, and green represent
540 pyroxene: white-yellow tones represent areas with spectra most like hedenbergite; green-gray
541 tones represent areas with spectra most like diopside. Red areas have spectra that match K-
542 feldspar. Blue areas have spectra matching quartz. Magenta areas have spectra matching
543 orthopyroxene (low-Ca pyroxene in “X-ray”). Black areas have spectra with no Raman peaks
544 (holes or fractures) or spectra that do not match pyroxene, quartz, or K-feldspar.

545
546

547 **Figure 5.** BSE images of typical occurrences of quartz with a hackle fracture pattern (**a.**) and
548 amorphous silica (**b.**) in sample 12001,909-14. The K-feldspar in **b.** is noticeably brighter in
549 contrast compared to the K-feldspar (**a.**) owing to its higher Ba content. The brightest phase in **a.**
550 is zirconolite; the brightest phase in **b.** is monazite.

551
552

553 **Figure 6.** BSE image mosaic of 12032,367-16 with high resolution BSE image inset (white
554 rectangle). In order of brightness from darkest to brightest, minerals are cristobalite, plagioclase,
555 K-feldspar, low-Ca pyroxene, apatite, ilmenite, and zircon. Zirconolite is the brightest phase but
556 is only visible as bright specks in the inset image.

557
558

559 **Figure 7.** BSE image mosaic of 12033,634-30. In order of brightness from darkest to brightest,
560 minerals (or phases) are quartz, plagioclase, K-feldspar, high-Ca pyroxene, low-Ca pyroxene,
561 apatite, RE-merrillite, olivine, ilmenite, zircon, and troilite.

562
563
564 **Figure 8.** BSE image mosaic of 12033,634-34. In order of brightness from darkest to brightest,
565 minerals (or phases) are quartz, plagioclase, ternary feldspar, K-feldspar, high-Ca pyroxene,
566 apatite, RE-merrillite, fayalite, ilmenite, and zircon. Zirconolite and baddeleyite are the brightest
567 phases and occur as elongate grains and specks, respectively.

568
569
570 **Figure 9.** Laser Raman spectra of quartz identified in samples 12001,909-14, 12023,147-10
571 (Seddio et al., 2014), 12033,634-30, 12033,634-34. K-feldspar peaks are present in quartz
572 spectra obtained from samples 12023,147-10 and 12033,634-30. We include quartz, orthoclase
573 (K-feldspar), cristobalite, and tridymite standard spectra from the RRUFF database (Downs,
574 2006) for comparison with our analyses.

575
576
577 **Figure 10.** Laser Raman spectra of cristobalite identified in sample 12032,367-16 that also
578 contains a contribution from nearby plagioclase. We include cristobalite, plagioclase
579 (oligoclase), tridymite, and quartz standard spectra from the RRUFF database (Downs, 2006) for
580 comparison with our analyses.

581
582
583 **Figure 11.** Laser Raman spectra of amorphous silica identified in sample 12001,909-14 that also
584 contains a contribution from nearby K-feldspar. We include orthoclase (K-feldspar), quartz,
585 cristobalite, and tridymite standard spectra from the RRUFF database (Downs, 2006) for
586 comparison with our analyses.

587
588
589 **Figure 12.** Concentrations of FeO and TiO₂ measured in silica by EPMA. Error bars represent
590 the “% error” calculated from counting statistics.

591

Table 1. Quantitative analyses of silica phases in granitic fragments from Apollo 12.

Sample	12001,		12001,		12023,		12032,		12033,		12033,	
Fragment	909-14		909-14		147-10		367-16		634-30		634-34	
Phase	Quartz		Amorph.		Quartz		Cristob.		Quartz		Quartz	
	wt%	σ	wt%	σ	wt%	σ	wt%	σ	wt%	σ	wt%	σ
SiO ₂	99.6	1.55	98.4	1.49	99.3	1.27	95.5	3.59	97.9	0.41	97.2	1.58
TiO ₂	0.15	0.06	0.20	0.02	0.10	0.02	0.49	0.13	0.16	0.06	0.11	0.06
Al ₂ O ₃	0.41	0.26	1.38	0.99	0.24	0.23	2.17	0.82	0.92	0.28	1.16	1.27
Cr ₂ O ₃	<0.02	-	<0.02	-	<0.02	-	<0.02	-	<0.02	-	<0.02	-
FeO	0.13	0.05	0.04	0.02	0.07	0.03	0.50	0.31	0.09	0.07	0.09	0.03
MgO	<0.01	-	<0.01	-	<0.01	-	<0.04	-	<0.01	-	<0.01	-
CaO	0.08	0.09	0.15	0.13	0.09	0.09	0.57	1.10	0.07	0.01	0.22	0.24
Na ₂ O	<0.02	-	0.14	0.09	<0.02	-	0.17	0.17	0.07	0.02	0.07	0.08
K ₂ O	0.06	0.07	0.40	0.59	0.03	0.02	0.33	0.34	0.28	0.20	0.27	0.38
P ₂ O ₅	<0.02	0.04	<0.02	0.01	<0.02	0.02	0.21	0.30	<0.02	0.02	<0.01	0.01
Sum	100.4		100.7		99.8		99.9		99.5		99.1	

“ σ ” is one standard deviation. “Amorph.” refers to amorphous silica. “Cristob.” refers to cristobalite.

Table 2. Modal abundances of 12001,909-14 areas.

Area	1	2	3	4	5	6	7
Silica	4.8	4.5	23	34	22	27	37
K-feldspar	13	29.5	27	29	15	24	46
Plagioclase	37	34	30	26	41	30	15
High-Ca Pyroxene	16	11	5.3	3.4	8.0	10	Trace
Low-Ca Pyroxene	27	19	13	5.0	9.5	3.6	0.8
Ilmenite	1.1	2.0	1.0	0.5	0.9	3.8	0.4
Ca-Phos.	1.1	-	0.4	0.3	2.4	1.1	-
Zircon	Trace	-	Trace	1.2	0.1	Trace	Trace
Zirconolite	-	-	-	-	Trace	-	-
Monazite	-	-	-	-	-	-	Trace

All values are in vol%. "Ca-Phos." refers to apatite and/or RE-merrillite. "-" means that the phase is not present in the area. Areas are depicted in Figure 3.

Table 3. Average compositions of major minerals in Areas 1 and 2 of sample 12001,909-14.

N	Area 1								Area 2							
	Kfs		Pl		High Ca Px		Low Ca Px		Kfs		Pl		High Ca Px		Low Ca Px	
	An _{1.1-15} Ab ₁₂₋₁₉ Or ₆₅₋₈₆ Cn _{1.2-1.5}		An ₅₀₋₈₄ Ab ₁₅₋₄₈ Or _{0.4-1.8} Cn _{<0.09}		En ₃₄₋₃₇ Fs ₂₈₋₃₉ Wo ₂₃₋₃₈		En ₄₀₋₄₂ Fs ₄₉₋₅₃ Wo _{6.3-9.7}		An _{3.7-26} Ab ₁₂₋₂₄ Or ₄₉₋₈₃ Cn _{0.9-1.8}		An ₃₈₋₈₆ Ab ₁₃₋₄₉ Or _{0.3-17} Cn _{<0.2}		En _{~34} Fs _{~27} Wo _{~39}		En ₄₂₋₄₃ Fs ₅₀₋₅₁ Wo _{5.9-7.9}	
17		22		2		6		7		5		1		5		
	wt%	σ	wt%	σ	wt%	σ	wt%	σ	wt%	σ	wt%	σ	wt%	σ	wt%	σ
SiO ₂	64.9	1.58	51.8	2.44	51.8	0.57	51.0	0.38	62.0	1.41	51.1	4.67	51.1	-	51.2	0.95
TiO ₂	0.08	0.03	0.05	0.02	0.71	0.08	0.37	0.04	0.10	0.06	0.08	0.04	0.79	-	0.39	0.13
Al ₂ O ₃	20.2	1.35	31.3	1.93	0.95	0.17	0.61	0.58	20.6	2.25	31.9	4.11	1.80	-	0.54	0.15
Cr ₂ O ₃	n.a.	-	n.a.	-	0.34	0.02	0.20	0.03	n.a.	-	n.a.	-	0.41	-	0.20	0.02
FeO	0.45	0.05	0.66	0.23	20.3	4.6	30.4	0.84	0.84	0.66	0.47	0.15	16.0	-	30.1	0.48
MnO	<0.03	-	<0.03	-	0.33	0.01	0.45	0.02	<0.03	-	<0.03	-	0.24	-	0.44	0.03
MgO	<0.01	-	0.07	0.11	12.1	0.64	13.8	0.24	0.31	0.41	0.06	0.05	11.5	-	14.3	0.18
CaO	1.49	1.38	13.8	1.95	14.6	5.02	3.71	0.56	4.04	3.00	13.4	5.42	18.0	-	3.16	0.37
BaO	0.75	0.08	<0.06	-	n.a.	-	n.a.	-	0.60	0.28	0.32	0.22	n.a.	-	n.a.	-
Na ₂ O	1.77	0.38	3.53	1.02	0.09	0.03	<0.02	-	2.48	1.45	2.60	1.63	0.21	-	0.05	0.03
K ₂ O	13.1	1.75	0.15	0.08	n.a.	-	<0.01	-	9.77	4.53	1.77	3.66	n.a.	-	0.05	0.04
P ₂ O ₅	n.a.	-	n.a.	-	<0.03	-	<0.04	-	n.a.	-	n.a.	-	0.06	-	0.17	0.18
Sum	102.7	-	101.4	-	101.2	-	100.5	-	100.7	-	101.7	-	100.1	-	100.6	-

Areas 1 and 2 refer to the areas shown in Fig. 3. “N” refers to the number of analyses averaged. “Kfs” refers to K-feldspar. “Pl” refers to plagioclase. “Px” refers to pyroxene. “Cn” refers to celsian—the Ba-feldspar end-member. “n.a.” means “not analyzed.”

Table 4. Average compositions of major minerals in Areas 3 and 4 of sample 12001,909-14.

	Area 3						Area 4										
	Kfs		Pl		High Ca Px		Low Ca Px		Kfs		Pl		High Ca Px		Low Ca Px		
	wt%	σ	An ₆₈₋₈₇ Ab ₁₃₋₃₁ Or _{0.4-1.2} Cn _{<0.1}	En ₃₃ Fs ₂₈ Wo ₃₉	En ₄₁ Fs ₅₁ Wo ₇₋₇	En _{6.7-11} Ab ₁₉₋₂₁ Or ₁₆₆₋₇₁ Cn _{2.0-2.7}	An ₆₄₋₈₉ Ab ₁₀₋₃₄ Or _{0.5-1.3} Cn _{<0.1}	En ₃₂ Fs ₂₈ Wo ₄₀	En ₄₁ Fs ₅₁₋₅₂ Wo _{7.7-8.7}	wt%	σ	An _{6.7-11} Ab ₁₉₋₂₁ Or ₁₆₆₋₇₁ Cn _{2.0-2.7}	En ₆₄₋₈₉ Ab ₁₀₋₃₄ Or _{0.5-1.3} Cn _{<0.1}	En ₃₂ Fs ₂₈ Wo ₄₀	En ₄₁ Fs ₅₁₋₅₂ Wo _{7.7-8.7}	wt%	σ
N	3	5	1	1	2	5	1	2	5	1	2	5	1	2	5	1	2
SiO ₂	63.1	1.07	49.2	1.68	50.7	-	50.1	-	63.5	1.34	49.4	2.67	50.9	-	49.9	0.28	
TiO ₂	0.09	0.02	0.08	0.03	0.86	-	0.46	-	0.07	0.07	0.06	0.03	0.83	-	0.36	0.01	
Al ₂ O ₃	20.7	1.10	33.3	1.32	1.03	-	0.41	-	20.7	0.28	32.8	2.00	0.84	-	0.36	0.01	
Cr ₂ O ₃	n.a.	-	n.a.	-	0.37	-	0.15	-	<0.04	-	<0.04	-	0.28	-	0.18	0.02	
FeO	0.18	0.03	0.41	0.07	17.1	-	30.9	-	0.15	0.06	0.30	0.03	16.7	-	30	0.14	
MnO	<0.04	-	<0.02	-	0.29	-	0.48	-	<0.05	-	<0.06	-	0.25	-	0.43	0.02	
MgO	<0.01	-	<0.03	-	11.1	-	13.6	-	<0.01	-	0.03	0.02	10.9	-	13.5	0.21	
CaO	1.73	1.12	15.8	1.36	18.2	-	3.58	-	1.79	0.59	15.5	2.04	18.7	-	3.77	0.4	
BaO	1.45	0.18	<0.06	-	<0.09	-	<0.08	-	1.32	0.30	<0.08	-	<0.08	-	<0.08	-	
Na ₂ O	2.24	0.31	2.40	0.71	0.09	-	<0.03	-	2.28	0.16	2.65	1.15	0.14	-	0.03	0.01	
K ₂ O	12.0	1.32	0.13	0.06	0.04	-	<0.01	-	11.8	0.64	0.14	0.06	0.07	-	0.05	0.04	
P ₂ O ₅	n.a.	-	n.a.	-	<0.05	-	<0.05	-	<0.03	-	0.05	0.01	<0.04	-	<0.04	-	
Sum	101.5	-	101.3	-	99.8	-	99.7	-	101.6	-	100.9	-	99.6	-	98.6	-	

Areas 3 and 4 refer to the areas shown in Fig. 3. “N” refers to the number of analyses averaged. “Kfs” refers to K-feldspar. “Pl” refers to plagioclase. “Cn” refers to celsian—the Ba-feldspar end-member. “Px” refers to pyroxene. “n.a.” means “not analyzed.”

Table 5. Average compositions of major minerals in Areas 5 and 6 of sample 12001,909-14.

	Area 5						Area 6											
	Kfs		Pl		High Ca Px		Low Ca Px		Kfs		Pl		High Ca Px		Low Ca Px			
	wt%	σ	An ₄₇₋₈₇ Ab ₁₂₋₄₈ Or _{0.2-5.1} Cn _{<0.1}	wt%	σ	En ₃₃₋₃₆ Fs _{2.6-3.4} Wo _{0.33-0.39}	wt%	σ	En ₃₉₋₄₃ Fs _{4.7-5.2} Wo _{0.7,2-1.2}	An _{1,2-3.1} Ab ₁₁₋₂₂ Or ₅₃₋₈₄ Cn _{1,2-4.0}	wt%	σ	An ₅₆₋₈₉ Ab ₁₁₋₄₂ Or _{0.1-1.8} Cn _{<0.1}	wt%	σ	En ₁₀₋₃₅ Fs _{2.7-4.9} Wo _{0.37-0.42}	wt%	σ
N	3	15	8	11	12	21	52	6										
SiO ₂	64.0	0.97	49.0	2.62	51.3	0.95	50.7	0.86	63.6	2.21	49.0	2.43	49.9	1.34	51.1	0.97		
TiO ₂	0.11	0.02	0.05	0.02	0.79	0.22	0.46	0.15	0.13	0.12	0.21	0.15	0.85	0.10	0.41	0.12		
Al ₂ O ₃	20.8	0.72	33.6	2.12	1.12	0.44	0.59	0.24	20.3	1.36	33.4	1.84	0.90	0.14	0.81	0.99		
Cr ₂ O ₃	n.a.	-	n.a.	-	0.38	0.10	0.23	0.08	n.a.	-	n.a.	-	0.21	0.13	0.17	0.05		
FeO	0.29	0.04	0.26	0.10	17.0	1.48	29.5	1.25	0.23	0.17	0.34	0.15	20.9	4.20	29.7	1.6		
MnO	<0.03	-	<0.03	-	0.26	0.03	0.44	0.03	<0.03	-	<0.04	-	0.29	0.05	0.45	0.05		
MgO	<0.01	-	0.03	0.01	11.6	0.32	13.9	0.38	0.10	0.10	0.03	0.01	8.07	2.97	13.7	0.73		
CaO	1.87	0.68	16.2	2.14	17.6	1.50	4.21	0.68	1.62	1.82	16.0	1.83	18.5	0.43	3.38	1.36		
BaO	1.19	0.07	<0.06	-	n.a.	-	n.a.	-	1.39	0.53	0.07	0.01	n.a.	-	n.a.	-		
Na ₂ O	2.03	0.19	2.24	1.07	0.12	0.01	0.05	0.04	1.82	0.34	2.34	0.98	0.10	0.02	<0.02	-		
K ₂ O	12.1	0.90	0.14	0.20	n.a.	-	<0.01	-	12.6	1.77	0.11	0.07	0.08	0.12	n.a.	-		
P ₂ O ₅	n.a.	-	n.a.	-	0.03	0.02	<0.02	-	n.a.	-	n.a.	-	0.03	0.02	0.03	0.02		
Sum	102.4	-	101.5	-	100.2	-	100.1	-	101.8	-	101.5	-	99.8	-	99.8	-		

Areas 5 and 6 refer to the areas shown in Fig. 3. “N” refers to the number of analyses averaged. “Kfs” refers to K-feldspar. “Pl” refers to plagioclase. “Px” refers to pyroxene. “Cn” refers to celtsian—the Ba-feldspar end-member. “n.a.” means “not analyzed.”

Table 6. Average compositions of major minerals in Area 7 of sample 12001,909-14.

	Area 7					
	Kfs		Pl		Low Ca Px	
	An _{0.8-13} Ab ₁₃₋₁₈ Or ₅₃₋₈₄ Cn _{3.1-5.1}		An ₄₃₋₄₆ Ab ₅₁₋₅₃ Or _{1.9-5.7} Cn _{<0.3}		En ₋₃₉ Fs ₋₅₃ Wo _{-7.6}	
N	10		4		1	
	wt%	σ	wt%	σ	wt%	σ
SiO ₂	64.5	1.06	58.4	0.74	50.3	-
TiO ₂	0.06	0.02	0.04	0.01	0.35	-
Al ₂ O ₃	19.9	0.62	27.2	0.21	0.39	-
Cr ₂ O ₃	n.a.	-	n.a.	-	0.17	-
FeO	0.05	0.02	0.16	0.02	30.9	-
MnO	<0.03	-	<0.03	-	0.49	-
MgO	<0.01	-	0.04	0.02	13.0	-
CaO	0.63	0.71	9.20	0.21	3.49	-
BaO	2.30	0.34	0.11	0.06	<0.09	-
Na ₂ O	1.69	0.23	5.89	0.03	<0.03	-
K ₂ O	13.4	0.79	0.58	0.31	0.07	-
P ₂ O ₅	n.a.	-	n.a.	-	<0.05	-
Sum	102.5	-	101.6	-	99.2	-

Area 7 refers to the area shown in Fig. 3. “N” refers to the number of analyses averaged. “Kfs” refers to K-feldspar. “Pl” refers to plagioclase. “Px” refers to pyroxene. “Cn” refers to celsian—the Ba-feldspar end-member. “n.a.” means “not analyzed.”

Table 7. Average compositions of major minerals in sample 12032,367-16.

	Kfs		Pl		Low Ca Px	
	An _{4.0-8.8} Ab ₁₈₋₂₁ Or ₆₅₋₇₂ Cn _{5.0-5.6}		An ₈₀₋₈₈ Ab ₁₁₋₁₈ Or _{0.2-5.8} Cn _{<0.3}		En ₅₂₋₅₉ Fs ₃₁₋₃₈ Wo _{3.5-17}	
N	2		8		6	
	wt%	σ	wt%	σ	wt%	σ
SiO ₂	63.8	0.78	46.8	1.31	52.9	0.57
TiO ₂	0.14	0.01	0.07	0.02	0.51	0.11
Al ₂ O ₃	20.9	1.63	34.4	0.58	0.59	0.16
Cr ₂ O ₃	<0.05	-	n.a.	-	0.25	0.05
FeO	0.13	0.01	0.22	0.10	22.4	1.59
MnO	<0.05	-	<0.03	-	0.33	0.02
MgO	<0.02	-	0.03	0.02	19.4	0.99
CaO	1.18	0.54	17.2	0.58	4.15	2.29
BaO	2.73	0.42	<0.08	-	<0.08	-
Na ₂ O	2.01	0.01	1.64	0.29	0.03	0.02
K ₂ O	10.8	1.56	0.22	0.32	<0.01	-
P ₂ O ₅	<0.05	-	<0.04	-	<0.05	-
Nb ₂ O ₅	n.a.	-	n.a.	-	n.a.	-
Sum	101.7	-	100.6	-	100.6	-

“N” refers to the number of analyses averaged. “Kfs” refers to K-feldspar. “Pl” refers to plagioclase. “Px” refers to pyroxene. “Cn” refers to celsian—the Ba-feldspar end-member. “n.a.” means “not analyzed.”

Table 8. Average compositions of major minerals in sample 12033,634-30.

	Kfs		Pl		High Ca Px		Low Ca Px		Ol		Ilm	
N	17		22		2		6		6		5	
	An _{0.7-14} Ab ₁₃₋₃₂ Or ₅₂₋₈₃ Cn _{2.3-4.9}		An ₄₄₋₆₅ Ab ₃₄₋₅₃ Or _{0.8-3.0} Cn _{<0.2}		En ₂₅₋₂₉ Fs ₃₃₋₃₈ Wo ₃₆₋₃₉		En ₃₀₋₃₂ Fs ₆₀₋₆₃ Wo _{5.7-10}		Fo ₂₀₋₂₂		Mg' _{2.9-4.2}	
	wt%	σ	wt%	σ	wt%	σ	wt%	σ	wt%	σ	wt%	σ
SiO ₂	63.1	1.23	54.4	2.12	50.5	1.16	49.8	0.68	31.7	0.3	<0.02	-
TiO ₂	0.07	0.02	0.05	0.02	0.95	0.5	0.48	0.21	0.28	0.03	52.6	0.92
Al ₂ O ₃	19.9	0.93	29.2	1.39	0.75	0.2	0.28	0.1	<0.02	-	<0.02	-
Cr ₂ O ₃	n.a.	-	n.a.	-	0.05	0.01	0.03	0.01	<0.02	-	0.08	0.03
FeO	0.18	0.12	0.27	0.1	22.5	1.65	34.7	1.88	59.0	0.26	44.9	0.24
MnO	<0.03	-	<0.03	-	0.34	0.05	0.54	0.05	0.58	0.03	0.42	0.04
MgO	<0.01	-	<0.01	-	8.96	0.51	10.1	0.56	8.89	0.27	1.04	0.09
CaO	0.96	0.91	11.4	1.57	16.5	1.76	4.89	2.25	0.05	0.01	0.06	0.03
BaO	1.81	0.38	<0.06	-	n.a.	-	n.a.	-	n.a.	-	n.a.	-
Na ₂ O	2.05	0.62	4.92	0.85	0.1	0.02	0.04	0.01	<0.03	-	<0.03	-
K ₂ O	12.7	1.63	0.21	0.08	<0.01	-	<0.01	-	0.03	0.01	n.a.	-
P ₂ O ₅	n.a.	-	n.a.	-	n.a.	-	n.a.	-	n.a.	-	n.a.	-
Nb ₂ O ₅	n.a.	-	n.a.	-	n.a.	-	n.a.	-	n.a.	-	0.68	0.4
Sum	100.8	-	100.5	-	100.7	-	100.9	-	100.5	-	99.8	-

“N” refers to the number of analyses averaged. “Kfs” refers to K-feldspar. “Pl” refers to plagioclase. “Px” refers to pyroxene. “Ol” refers to olivine. “Ilm” refers to ilmenite. “Cn” refers to celsian—the Ba-feldspar end-member. “n.a.” means “not analyzed.”

Table 9. Average compositions of major minerals in sample 12033,634-34.

	Kfs		Tfs		Pl		High Ca Px		Ol		Ilm	
N	15		26		2		6		6		5	
	An _{2.2-18} Ab ₁₂₋₂₈ Or ₅₁₋₈₀ Cn _{2.3-8.0}		An ₂₈₋₅₂ Ab ₂₃₋₂₉ Or ₂₅₋₄₁ Cn _{<0.1-4.9}		An ₄₉₋₅₁ Ab ₄₇₋₄₉ Or _{1.1-1.7} Cn _{<0.2}		En ₁₆₋₂₀ Fs ₄₀₋₄₃ Wo ₄₀₋₄₁		Fo _{9.0-13}		Mg' _{0.8-1.1}	
	wt%	σ	wt%	σ	wt%	σ	wt%	σ	wt%	σ	wt%	σ
SiO ₂	63.3	1.01	55.5	2.28	54.0	1.56	48.9	0.42	30.9	0.32	<0.02	-
TiO ₂	0.05	0.02	0.04	0.02	0.05	0.02	1.27	0.08	0.14	0.10	51.8	0.27
Al ₂ O ₃	19.2	0.75	25.6	1.38	27.5	0.68	1.38	0.18	<0.02	-	<0.02	-
Cr ₂ O ₃	n.a.	-	n.a.	-	n.a.	-	0.03	0.01	<0.02	-	<0.02	-
FeO	0.58	0.35	1.56	1.92	0.79	0.09	24.3	0.69	64.8	1.20	46.2	0.80
MnO	0.03	0.00	0.08	0.04	<0.04	-	0.35	0.02	0.76	0.08	0.39	0.01
MgO	<0.02	-	<0.02	-	<0.03	-	5.76	0.44	4.27	0.62	0.25	0.03
CaO	1.48	0.89	7.92	1.55	10.3	0.32	18.3	0.12	0.20	0.08	0.06	0.01
BaO	2.46	0.66	0.87	0.79	0.09	0.03	n.a.	-	n.a.	-	n.a.	-
Na ₂ O	1.85	0.47	2.60	0.31	5.50	0.16	0.10	0.02	<0.03	-	<0.03	-
K ₂ O	10.6	1.68	4.63	0.44	0.25	0.07	<0.02	-	<0.02	-	n.a.	-
P ₂ O ₅	n.a.	-	n.a.	-	n.a.	-	n.a.	-	n.a.	-	<0.02	-
Nb ₂ O ₅	n.a.	-	n.a.	-	n.a.	-	n.a.	-	n.a.	-	0.53*	0.04*
Sum	99.6	-	98.8	-	98.5	-	100.3	-	101.1	-	99.2	-

*Nb₂O₅ was measured for only two of the analyses. “N” refers to the number of analyses averaged. “Kfs” refers to K-feldspar. “Tfs” refers to ternary feldspar. “Pl” refers to plagioclase. “Px” refers to pyroxene. “Ol” refers to olivine. “Ilm” refers to ilmenite. “Cn” refers to celsian—the Ba-feldspar end-member. “n.a.” means “not analyzed.”

Table 10. Raman peak positions for identified phases.

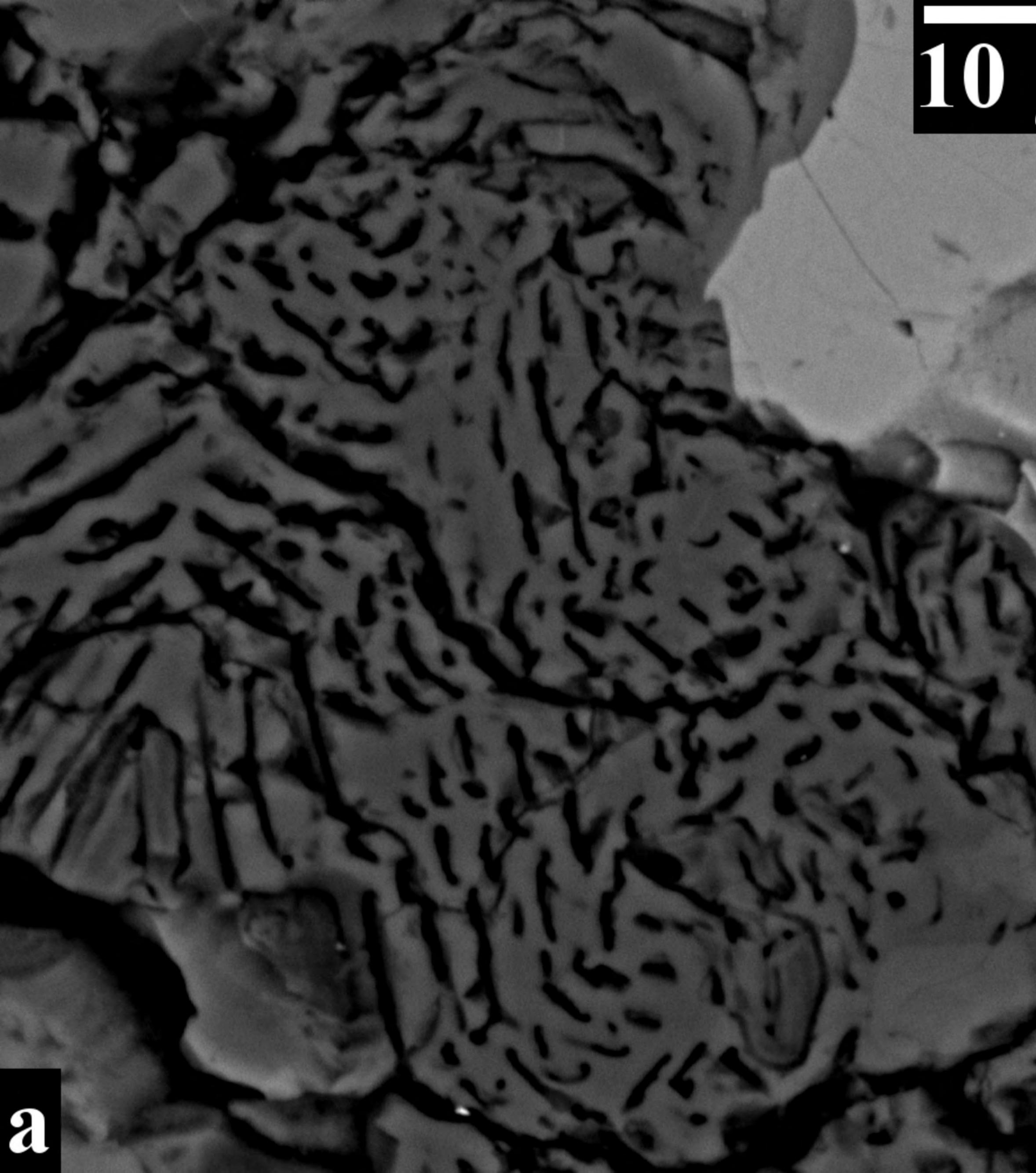
Sample	Phase	Peaks used for identification (cm ⁻¹)	
12001,909-14	Quartz	463	353
	K-feldspar	512	472
12023,147-10	Quartz	463	-
	K-feldspar	513	-
12032,637-16	Cristobalite	415	229
	Plagioclase	508	481
12033,634-30	Quartz	462	-
	K-feldspar	513	476
12033,634-34	Quartz	460	-
	Quartz	464	358
	Cristobalite	418	230
Reference	K-feldspar	513	474
	Plagioclase (oligoclase)	508	480

We include quartz, orthoclase (K-feldspar), cristobalite, and tridymite standard spectra from the RRUFF database (Downs, 2006; Ling et al., 2011) for comparison with our analyses.

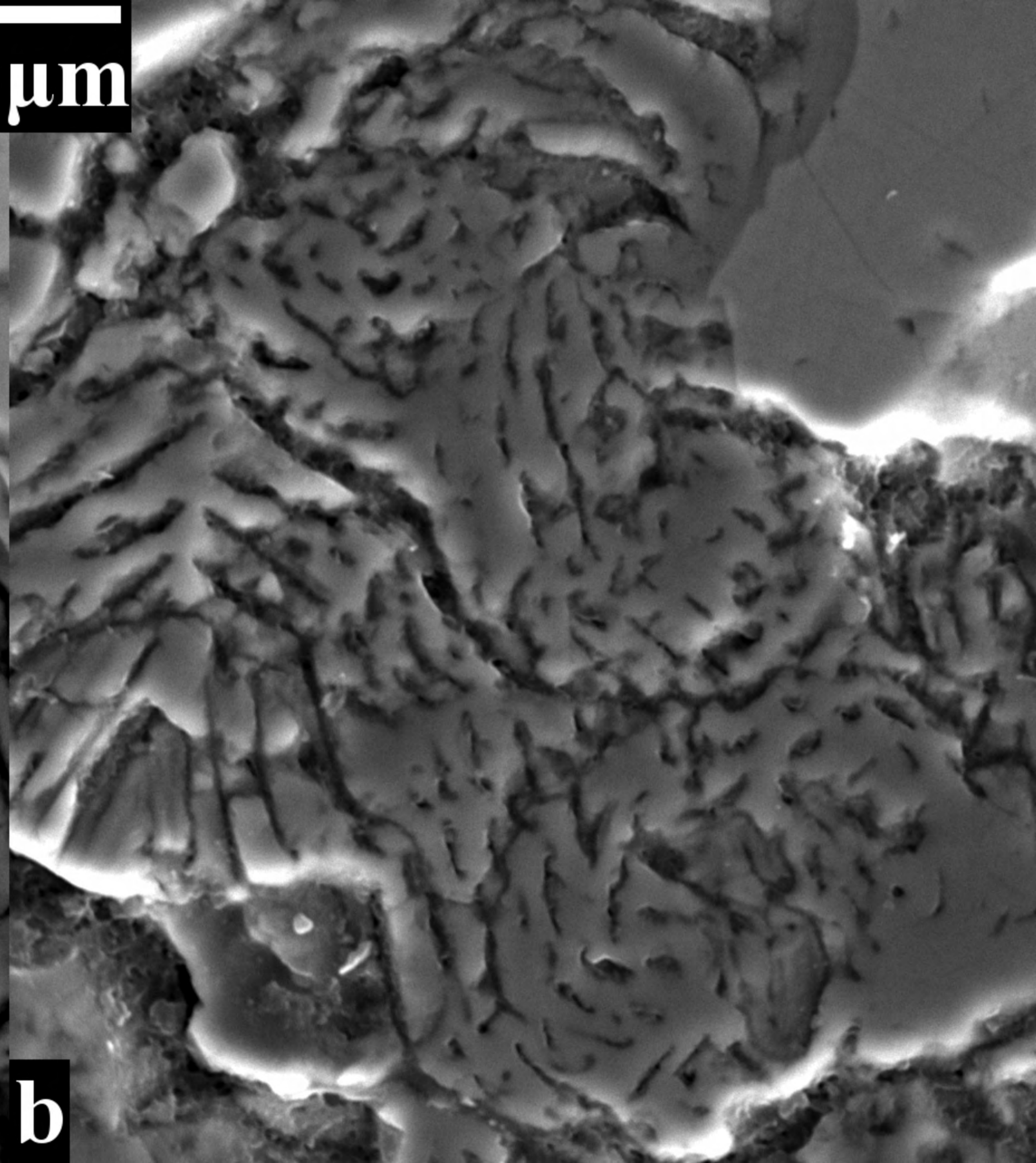
Table 11. Initial density calculation.

Sample	12001,	12023,	12032,	12033,	12033,
Fragment	909-14	147-10	366-19	634-30	634-34
Phase	Quartz	Quartz	Quartz	Quartz	Quartz
ρ_q	2.65	2.65	2.65	2.65	2.65
ρ_i	2.21	2.17	2.18	2.23	2.43
σ	0.01	0.02	0.05	-	0.04
$\rho_{\text{trid.}}$	2.18–2.28				
$\rho_{\text{crist.}}$	2.32–2.36				

Results of the initial density calculation (see text) for quartz with a hackle fracture pattern. “ ρ_q ” refers to the assumed density of quartz used in the calculation. “ ρ_i ” refers to the calculated initial density for the silica in each sample and is an average of calculated initial densities from multiple secondary electron images for all samples except for 12033,634-30, from which only one high resolution secondary electron image was taken. “ σ ” is one standard deviation of the initial densities calculated from multiple secondary electron images of each sample. Densities of tridymite (Kihara, 1978) and cristobalite (Schmahl et al., 1992) are given for comparison. All values are in g/cm^3 .



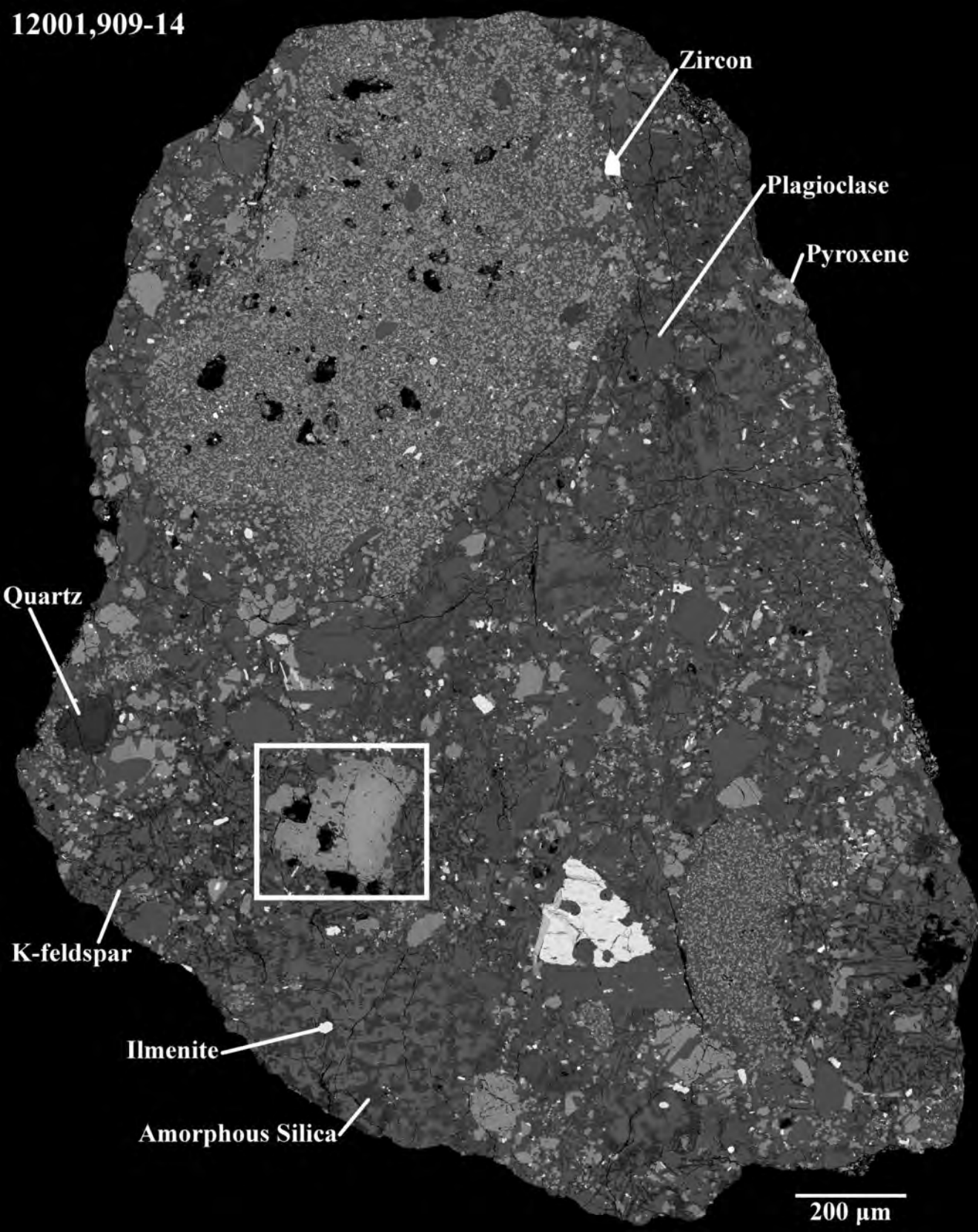
10 μm

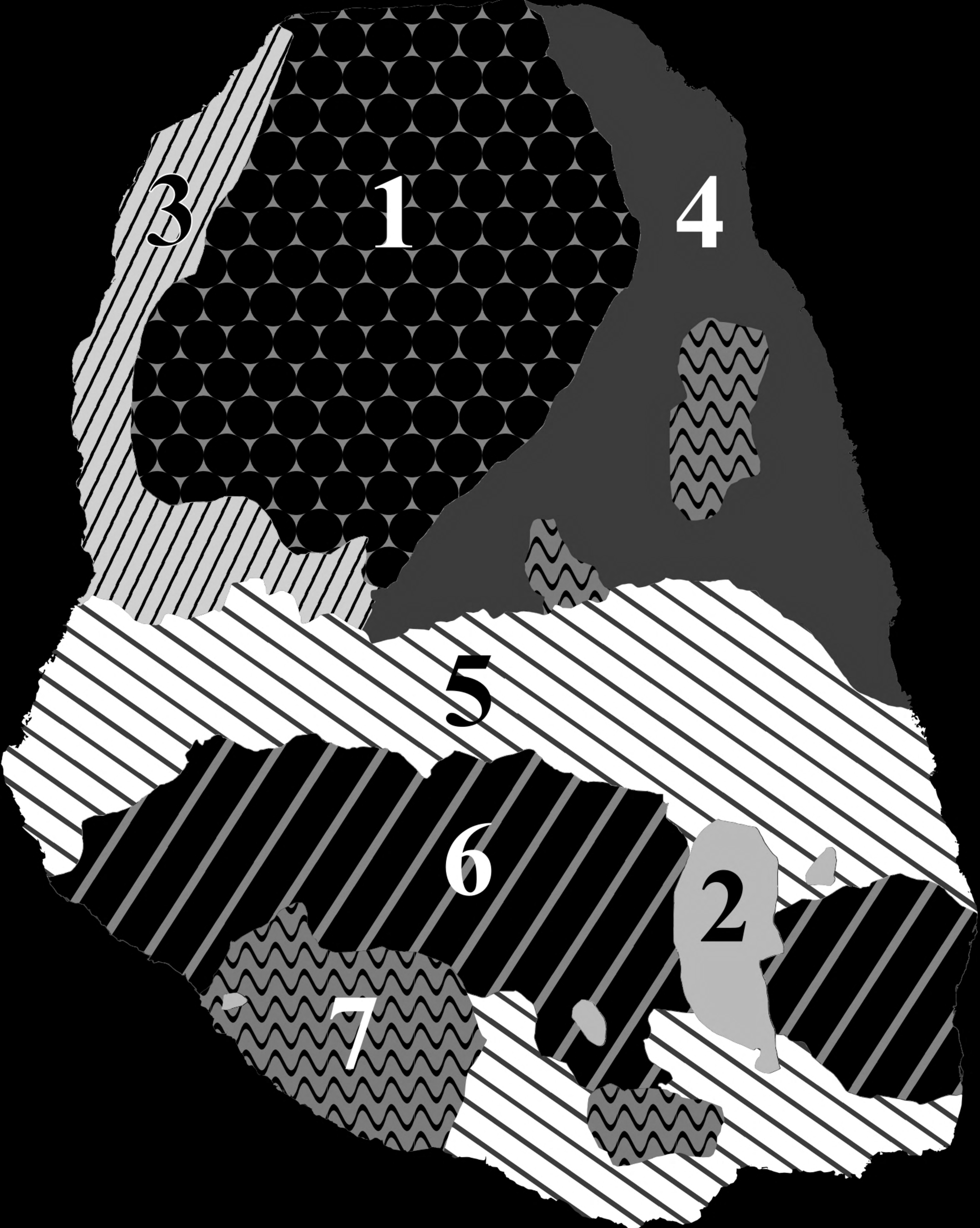


a

b

12001,909-14





3

1

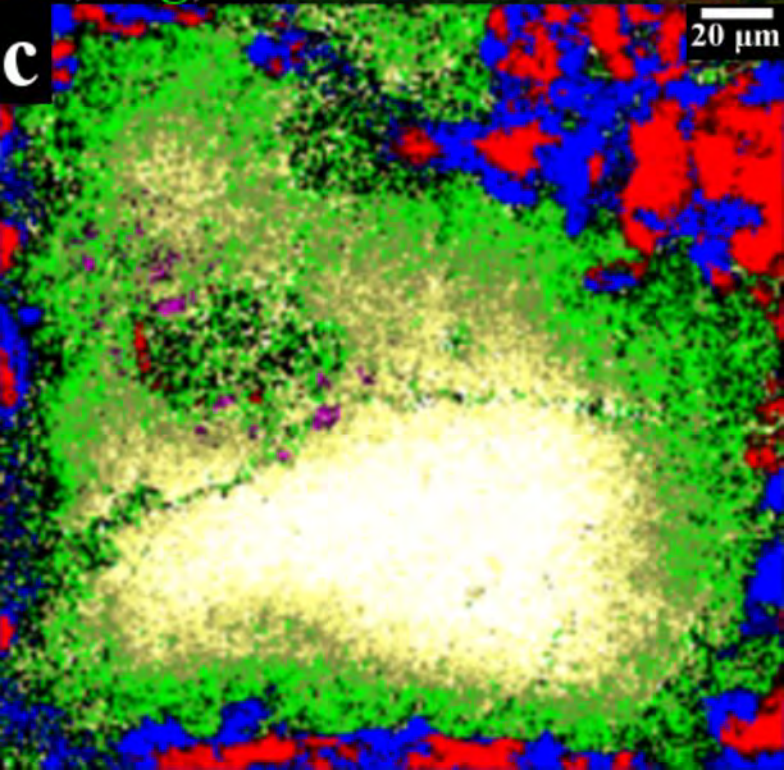
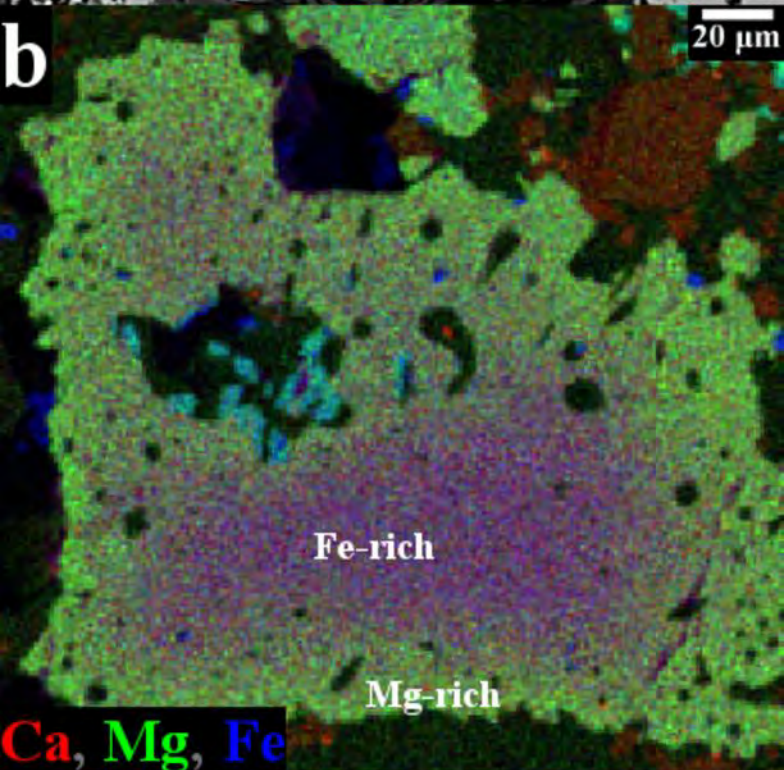
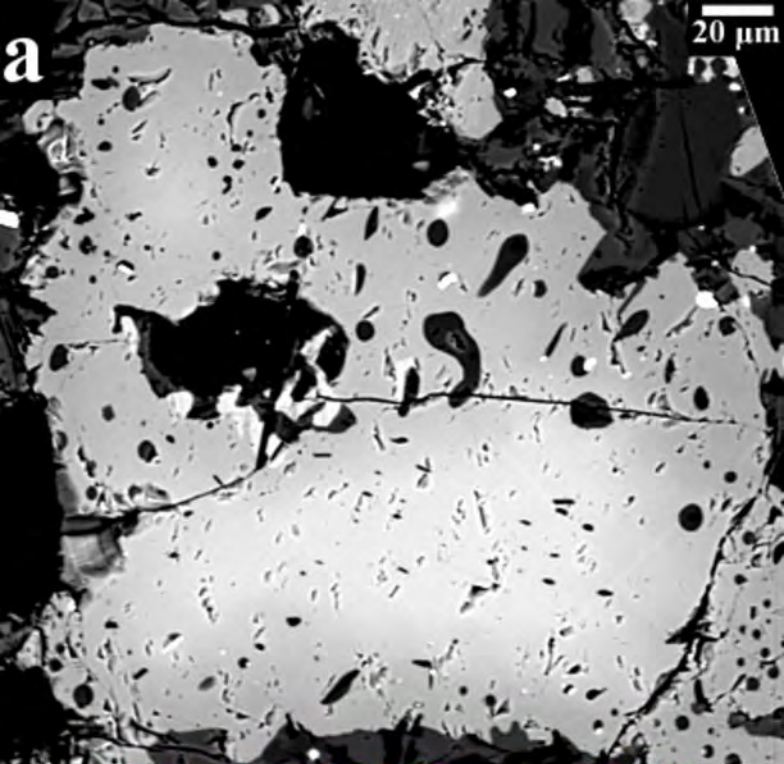
4

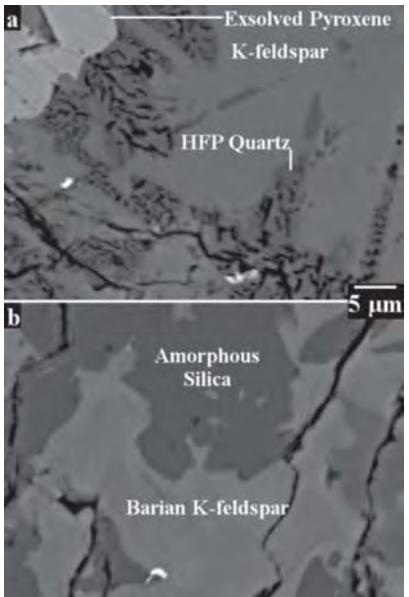
5

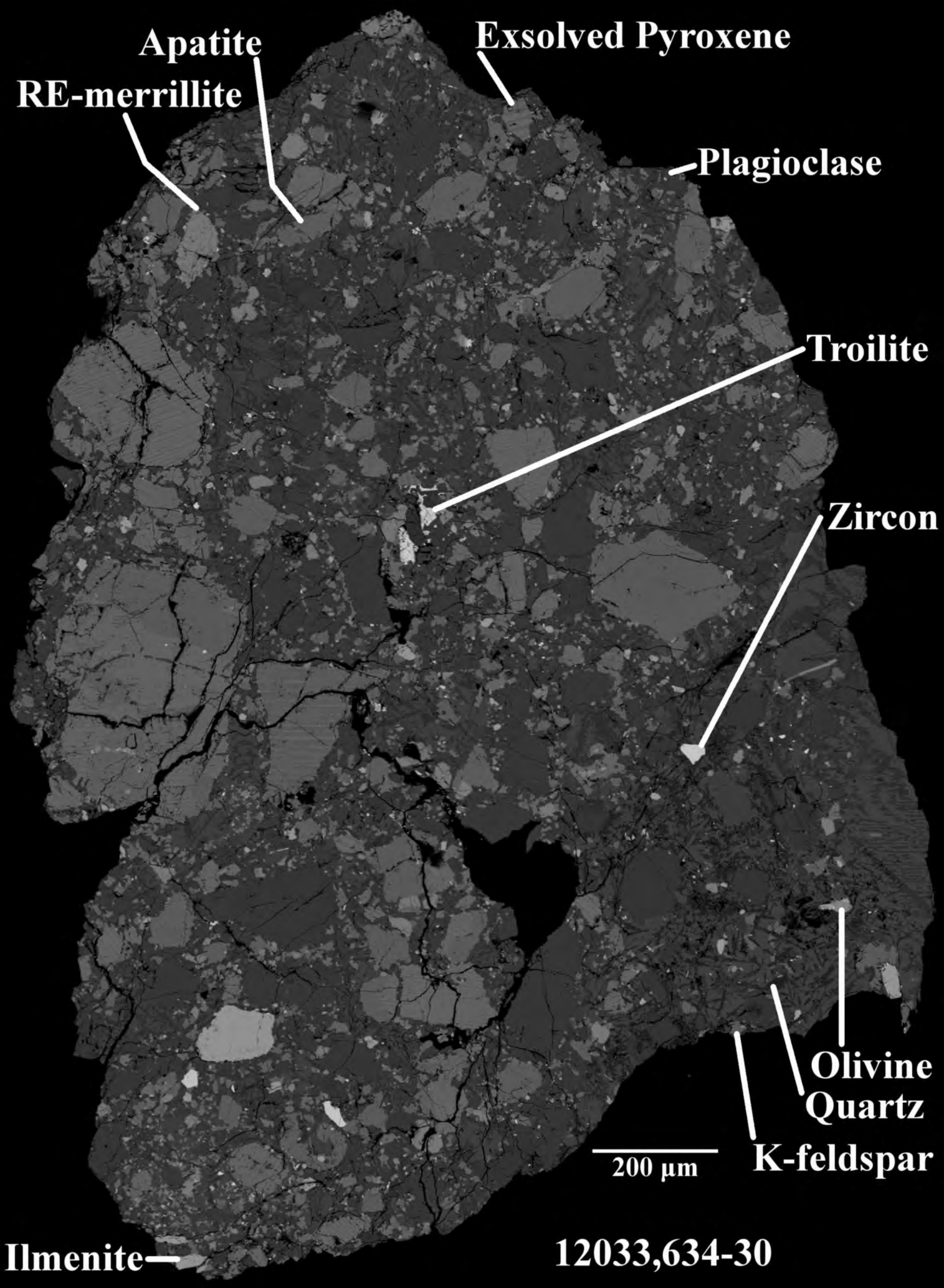
6

2

7







Apatite

RE-merrillite

Exsolved Pyroxene

Plagioclase

Troilite

Zircon

**Olivine
Quartz**

K-feldspar

200 μm

Ilmenite

12033,634-30

12033,634-34

